



Chinese Society of Aeronautics and Astronautics  
& Beihang University

Chinese Journal of Aeronautics

cja@buaa.edu.cn  
[www.sciencedirect.com](http://www.sciencedirect.com)



FULL LENGTH ARTICLE

# Numerical investigation on aerodynamic characteristics of equivalent distributed ducted propellers



Zeyu LI <sup>a,b</sup>, Jianghao WU <sup>c</sup>, Bairui PEI <sup>a,c</sup>, Long CHEN <sup>c</sup>, Zhengping ZOU <sup>d</sup>,  
Haiying LIN <sup>a,c,\*</sup>

<sup>a</sup> Hangzhou International Innovation Institute, Beihang University, Hangzhou 311115, China

<sup>b</sup> School of Energy and Power Engineering, Beihang University, Beijing 100191, China

<sup>c</sup> School of Transportation Science and Engineering, Beihang University, Beijing 100191, China

<sup>d</sup> Research Institute of Aero-engine, Beihang University, Beijing 100083, China

Received 16 December 2024; revised 7 February 2025; accepted 23 February 2025

Available online 14 March 2025

## KEYWORDS

Aerodynamic performance;  
Computational fluid dynamics;  
Distributed ducted propeller;  
Flow fields;  
Rotational consistency

**Abstract** Distributed ducted propellers hold significant promise for propulsion systems in Advanced Air Mobility (AAM) due to their high efficiency, low noise, and enhanced redundancy and safety. However, a standardized benchmark for comparing the aerodynamic characteristics of different ducted propeller configurations remains lacking. Including additional ducted propellers can further complicate the flow field. This paper proposes an equivalent design method for ducted propellers based on the momentum theorem and similarity criteria, introducing three equivalent ducted propeller cases. Transient numerical simulations are conducted using the sliding mesh model. The three cases produce comparable thrust while consuming the same power, with the volume of distributed ducted propellers being reduced by over 29% compared to the single ducted propeller. This study investigates the effect of rotational frequency on aerodynamic performance under hovering conditions. While propeller performance demonstrates low sensitivity to variations in rotational frequency, duct performance exhibits high sensitivity. The research further examines how rotational frequency changes the pressure difference between the duct leading edge and trailing edge. Based on a sensitivity analysis of aerodynamic performance, the flow field mechanisms under different rotational consistency are examined for the case with one duct and two propellers. Differences in aerodynamic performance are attributed to the airflow velocity gradient differences at the

\* Corresponding author.

E-mail address: [haiying@buaa.edu.cn](mailto:haiying@buaa.edu.cn) (H. LIN).

Peer review under responsibility of Editorial Committee of CJA



Production and hosting by Elsevier

duct leading edge and the flow separation characteristics on the crossing side. These findings are significant for enhancing the performance of distributed ducted propellers and improving aircraft controllability.

© 2025 The Author(s). Published by Elsevier Ltd on behalf of Chinese Society of Aeronautics and Astronautics. This is an open access article under the CC BY-NC-ND license (<http://creativecommons.org/licenses/by-nc-nd/4.0/>).

## 1. Introduction

In recent years, the rapid advancement of Advanced Air Mobility (AAM) has seen many electric Vertical Take-Off and Landing (eVTOL) aircraft, such as Lilium and VoloConnect, adopt ducted propellers as their propulsion systems.<sup>1</sup> Compared to open rotors, ducted propellers enclose the blades within a duct, using the inner wall to limit blade tip vortices and reduce the acoustic footprint of the propeller. This design offers lower noise, higher static aerodynamic efficiency, and improved structural safety,<sup>2</sup> albeit at the expense of increased weight and greater horizontal drag. Ducted propulsion systems can be configured in various ways, including distributed and single-ducted propulsion. Single-duct propulsion systems integrate the individual ducted propeller into the aircraft structure. In contrast, distributed ducted propulsion, exemplified by Lilium, features multiple closely positioned and aerodynamically integrated ducts on each wing.<sup>3</sup> Research on single ducted propellers dates back to the 1960s when NASA designed and tested multiple ducted propeller prototypes to evaluate the aerodynamic performance of tilting ducts mounted on wings.<sup>4</sup> Recent studies have primarily focused on examining the effects of parameterized design on the aerodynamic performance of ducted propellers, particularly in the context of Unmanned Aerial Vehicle (UAV) applications. Computational Fluid Dynamics (CFD) methods provide a cost-effective means to obtain more accurate and detailed aerodynamic performance data and flow field analysis results.<sup>5,6</sup> Li et al.<sup>7–9</sup> conducted theoretical research and numerical simulations on tip-jet ducted propellers. They proposed a rapid prototyping method for calculating jet torque using the momentum theorem. They analyzed ducted propellers' internal flow field characteristics through Unsteady Reynolds-Averaged Navier-Stokes (URANS) simulations. They elucidated how the Coandă effect blocks jet flow on the propeller, leading to increased propeller lift, and described the influence of design parameters on aerodynamic performance. Cao et al.<sup>10</sup> have investigated the effects of duct Leading Edge (LE) shapes on aerodynamic performance and proposed corresponding optimization strategies through numerical simulations. Luo et al.<sup>11–14</sup> employed the Sliding Mesh Model (SMM) transient simulations to evaluate the wind, wall, ground, and ceiling effects on ducted propellers, revealing changes in aerodynamic performance and underlying flow mechanisms. Zhao et al.<sup>15</sup> explored the ground effect on ducted propellers at various attitude angles with Multiple Reference Frame (MRF) model. Hu et al.<sup>16,17</sup> investigated multi-objective optimization methods for the geometric parameters of ducted propellers through numerical simulation and experimental approaches, achieving a hovering efficiency higher than that of open propellers. Focusing on hovering flight, Mi<sup>18</sup> conducted transient numerical simulations of near-ground and near-water effects of ducted propellers using the Volume of Fluid (VOF) method, uncovering the physical

characteristics of ducted propellers in multiphase asymmetric fields. Zhang et al.<sup>19</sup> conducted high-fidelity URANS simulations based on NASA test cases, proposing methods to design ducted propellers and propellers equivalently and providing detailed analyses of the aerodynamic and acoustic performance of these equivalent systems. However, there remains limited research on equivalent design methods and aerodynamic performance across different ducted propellers, especially when comparing single and distributed configurations. It is also necessary to elucidate their mechanisms based on flow field characteristics.

Distributed ducts represent an emerging frontier in distributed propulsion. Current numerical simulations of distributed propulsion mainly focus on the aerodynamic performance improvements brought by slipstream enhancement due to Boundary Layer Ingestion (BLI) on wings or Blended Wing Bodies (BWB).<sup>20</sup> Zhou et al.<sup>5,21–23</sup> proposed a computational approach based on Blade Element Momentum Theory (BEMT) and the panel method to evaluate the aerodynamic performance of integrated propeller-wing models. URANS simulations for validation and flow characteristic analysis revealed the coupling effects between adjacent propellers, adjacent ducts, and between propellers, ducts, and wings, as well as the propeller-induced slipstream enhancement above the wing. However, the MRF model could not fully capture the unsteady characteristics of this integrated model. Ma et al.<sup>24</sup> introduced reduced-order models and design methods for multiple ducted units in distributed propulsion, but simplifying mutual interference effects between ducts calls for further in-depth research. Experimental studies on distributed propulsion focus on the interference between multiple propeller units and parametric investigation. de Vries et al.<sup>25</sup> investigated the aerodynamic performance and flow field characteristics of three closely spaced side-by-side propellers through wind tunnel tests, evaluating the effects of parameters such as rotation direction, angle of attack, relative position, thrust difference, and phase angle. Zhang et al.<sup>26</sup> investigated the characteristics of vector propulsion integrated with distributed systems and wings using wind tunnel experiments, validating the accuracy of CFD simulations. Previous numerical and experimental studies have lacked standardized benchmarks for evaluating distributed ducted propellers and have rarely conducted detailed analyses of aerodynamic interference within such systems. High-fidelity transient CFD simulations contribute to more continuous and precise results. Additional studies based on equivalent design methodologies are necessary to comprehensively assess the performance of various ducted propeller designs in eVTOL power systems.

This research aims to parametrically evaluate the aerodynamic performance and flow field mechanisms of various configurations of ducted propellers. Based on similarity criteria, this paper proposes a set of equivalent ducted propeller cases with the same thrust-power ratio. Utilizing URANS numerical

methods, this paper analyzes their hovering performance and how it is affected by parameters such as tip Mach number ( $Ma_{tip}$ ) and rotational consistency. It also delves into the flow field mechanisms. The structure of the paper is as follows: [Section 2](#) details the theoretical model of equivalent ducted propellers and the setup of three case studies. [Section 3](#) outlines and validates the numerical and experimental methodologies. [Section 4](#) presents a comparative analysis of the aerodynamic performance across the three cases, elucidating the effects and mechanisms of the various parameters. [Section 5](#) concludes with a summary of the findings.

## 2. Numerical models

Eqs. (1)–(4) define the dimensionless parameters characterizing aerodynamic performance used in this paper.

Thrust coefficient:

$$C_T = \frac{T}{\rho n^2 D^4} \quad (1)$$

Power coefficient:

$$C_Q = \frac{P}{\rho n^3 D^5} = \frac{2\pi Q_p}{\rho n^2 D^5} \quad (2)$$

The figure of merit:

$$FoM = \frac{\sqrt{2} C_T^{\frac{3}{2}}}{\sqrt{\pi} C_Q} \quad (3)$$

Pressure coefficient:

$$C_p = \frac{8p}{\rho n^2 D^2} \quad (4)$$

where  $T$  represents the hovering thrust,  $\rho$  denotes the fluid density,  $n$  is the propeller rotational frequency,  $D$  is the propeller diameter,  $q$  represents the propeller torque,  $P$  is the propeller power, and  $p$  denotes the local pressure, respectively.

### 2.1. Model setup

The ducted propeller model utilized in this paper is derived from the prototype developed by our research team. [Fig. 1](#) illustrates the structure of the wind tunnel test model design-

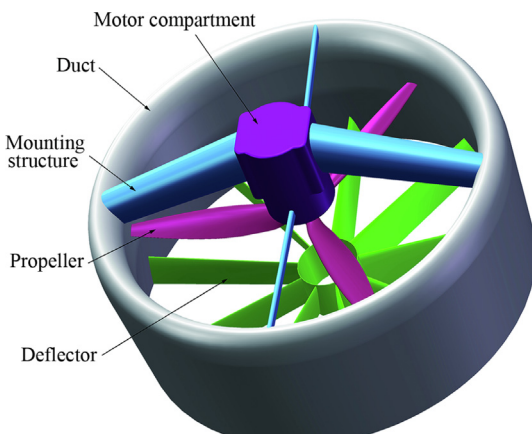


**Fig. 1** Case-WT model.

nated as Case-WT. The Case-WT configuration comprises a duct, propeller, deflector, motor compartment, and mounting structure. The lift system of Case-WT consists of a circular duct and a three-blade propeller based on the MH 112 airfoil. In contrast, the deflector features nine AG 24 airfoil blades affixed to the duct inner wall to counterbalance the torque produced by the propeller. The subsequent numerical studies adopt the baseline case with one duct and one propeller (Case-1D1P), simplifying the computational model. The blade sections' airfoil profile, twist angle, and chord length distribution are shown in [Fig. 2](#), where  $R^* = r/R$  and the centers of each  $R^*$  section align along a straight line. The shape of the duct section and the duct-propeller alignment for Case-1D1P are illustrated in [Fig. 3](#), with the corresponding geometric parameters outlined in [Table 1](#).

This study explores the performance of two distinct configurations of ducted propellers at varying tip Mach number and rotational consistency. For the case featuring two ducts and two propellers (Case-2D2P), the center-to-center distance is 2 times the duct's inner diameter, which ensures the ducts are sufficiently separated. In contrast, the center distance for the case with one duct and two propellers (Case-1D2P) is 1.02 times the duct inner diameter, with the ducts maintaining an intersecting common section and their LE merged. [Fig. 4](#) presents diagrams of Case-1D1P, Case-2D2P, and Case-1D2P, with numbers on the ducts indicating Sampling Points (SP) for subsequent pressure analysis. The conversion relationships for the diameters of the three cases are detailed in later sections. The green area represents the solid structure of the ducted propeller, and the purple zone represents the envelope cubic. The blue dashed rectangles indicate the envelope cubic settings for different cases.

### 2.2. Equivalent ducted propeller

An equivalent design method for ducted propellers is proposed to effectively evaluate the aerodynamic performance of different configurations under hovering conditions. Equivalent configurations refer to consuming identical power while generating the same thrust.<sup>19</sup> Firstly, the momentum theorem is applied to derive the thrust for Case-1D1P:

$$T_{1D1P} = \dot{m} V_{out} \quad (5)$$

where  $V_{out}$  represents the air velocity at the duct Trailing Edge (TE), and  $\dot{m}$  is the air mass flow rate at the propeller, defined as  $\dot{m} = A_{D11} \rho v_i$ , with  $v_i$  representing the induced velocity at the propeller and  $A_{D11}$  being the cross-sectional area of the duct at the propeller. Based on the principle of fluid continuity,  $V_{out}$  is related to the induced velocity  $v_i$  as follows:

$$v_i A_{D11} = V_{out} A_{out} \Rightarrow V_{out} = \frac{v_i}{\Delta} \quad (6)$$

where  $A_{out}$  is the cross-sectional area at the duct TE, and  $\Delta$  is the duct expansion ratio  $A_{out}/A_{D11}$ .

The thrust of the ducted propeller is given by

$$T_{1D1P} = \frac{A_{D11} \rho v_i^2}{\Delta_{1D1P}} \quad (7)$$

The power of the ducted propeller is:

$$P_{1D1P} = \frac{A_{D11} \rho v_i^3}{2 \Delta_{1D1P}^2} \quad (8)$$

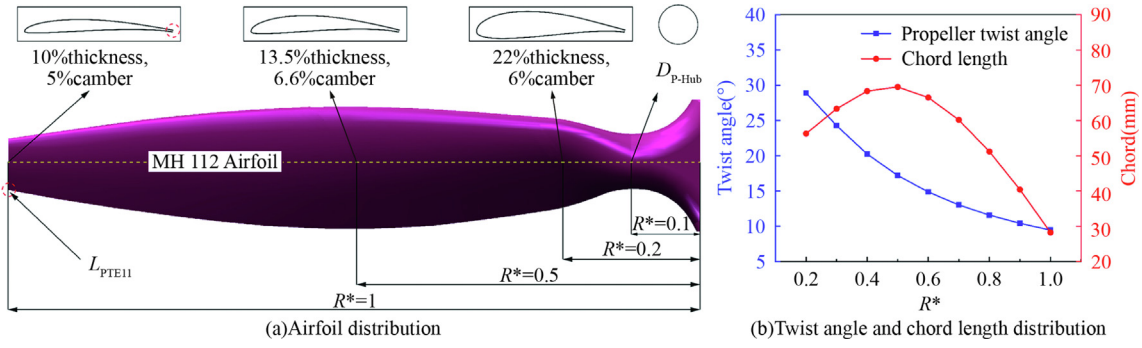


**Fig. 2** Propeller design parameters.

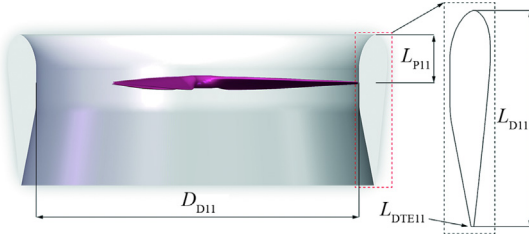


**Fig. 3** Sectional view of Case-1D1P model.

**Table 1** Physical geometric parameters for Case-1D1P.

Parameter	Value
$D_{D11}$ (m)	0.749
$L_{P11}$ (m)	0.11
$L_{D11}$ (m)	0.35
$L_{pTE11}$ (m)	0.000 4
$L_{DTE11}$ (m)	0.004
$L_{DP11}$ (m)	0.003

Rewriting Eqs. (7) and (8) in terms of the induced velocity as an intermediate variable, the relationship between thrust and power for the ducted propeller becomes

$$v_i = \sqrt{\frac{T_{1D1P}\Delta_{1D1P}}{A_{D11}\rho}} = \sqrt{\frac{2P_{1D1P}\Delta_{1D1P}^2}{A_{D11}\rho}} \quad (9)$$

Thus,

$$T_{1D1P} = P_{1D1P}^{2/3} \sqrt[3]{4\Delta_{1D1P} A_{D11}\rho} \quad (10)$$

where  $A_{D11} = \pi D_{D11}^2/4$  and  $D_{D11}$  is the duct cross-sectional diameter of Case-1D1P.

Similarly, for Case-1D2P, the relationship between thrust and power is given by

$$T_{1D2P} = f(P_{1D2P}) = P_{1D2P}^{2/3} \sqrt[3]{4\Delta_{1D2P} A_{D12}\rho} \quad (11)$$

where  $A_{D12} = \pi D_{D12}^2/2$  and  $D_{D12}$  is the duct cross-sectional diameter of Case-1D2P.

For Case-2D2P, the relationship between thrust and power is

$$T_{2D2P} = f(P_{2D2P}) = P_{2D2P}^{2/3} \sqrt[3]{4\Delta_{2D2P} A_{D22}\rho} \quad (12)$$

where  $A_{D22} = \pi D_{D22}^2/2$  and  $D_{D22}$  is the duct cross-sectional diameter of Case-2D2P, with  $\Delta_{2D2P} = \Delta_{1D1P}$ .

Eqs. (10) and (11) are identical, leading to a dimensional relationship between Case-1D1P and Case-1D2P:

$$D_{D12} = \sqrt{\frac{D_{D11}^2 \Delta_{1D1P}}{2\Delta_{1D2P}}} \quad (13)$$

Similarly, Eqs. (10) and (12) are equal, establishing the dimensional relationship between Case-1D1P and Case-2D2P:

$$D_{D22} = \sqrt{\frac{D_{D11}^2 \Delta_{1D1P}}{2\Delta_{2D2P}}} = \frac{\sqrt{2}}{2} D_{D11} \quad (14)$$

### 2.3. Geometric models based on similarity criteria

The loading conditions are adjusted according to similar criteria<sup>27</sup> to ensure a consistent power benchmark across the different cases. In this setup, all size parameters for the various cases are scaled proportionally, with the solidity of each configuration assumed to be identical. The rotational frequency ratio is the inverse of the size ratio, which guarantees that each case maintains the same tip Mach number.

Measurement results indicate that for Case-1D1P and Case-2D2P,  $\Delta_{1D2P} = \Delta_{1D1P} \approx 0.183\ 283$ , while for Case-1D2P,  $\Delta_{1D2P} \approx 0.192\ 934$ . From the calculations, the inner diameters of the ducts are determined to be  $D_{D22} \approx 0.529\ 6$  m,  $D_{D12} \approx 0.531\ 8$  m. Table 2 presents the comparison of geometric volume parameters across three cases. The shape envelope cubic volume considers only the external contour of the shape and excludes the gap between the Case-2D2P pairs.

## 3. Methodology

### 3.1. Numerical method

This study utilizes the Navier-Stokes (N-S) solver ANSYS Fluent, a commercially available tool based on the finite volume method, for URANS simulations. Using the Sutherland ideal gas model, the SST  $k-\omega$  turbulence model is employed to solve the N-S viscous fluid motion equations. A total energy model accounts for compressibility effects, and unsteady numerical simulations of the propeller's SMM are conducted. In contrast, an MRF model facilitates the initialization of steady calculations for rapid convergence. All computations rely on a

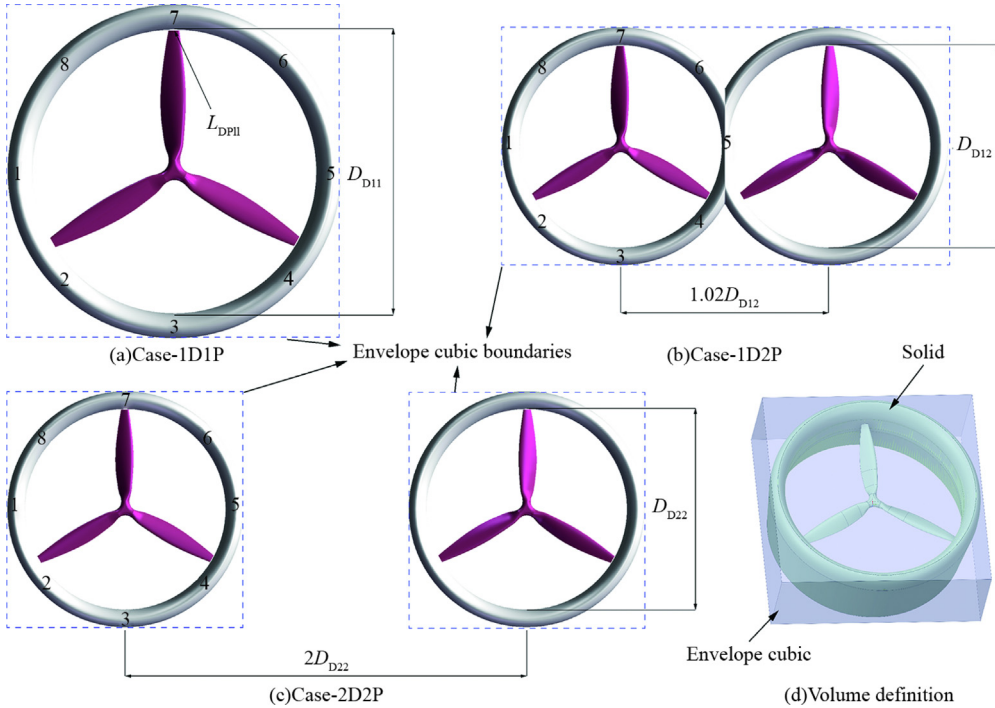


**Fig. 4** Ducted propeller geometry definitions.

**Table 2** Comparison of geometric volume parameters for three cases.

Parameter	Value		
	Case-1D1P	Case-1D2P	Case-2D2P
Total length along X-axis (m)	0.88	1.174	1.246
Total length along Y-axis (m)	0.88	0.625	0.623
Total length along Z-axis (m)	0.35	0.249	0.247
Shape envelope cubic volume ( $\text{m}^3$ )	0.271	0.182	0.192
The total solid volume ( $\text{m}^3$ )	0.039	0.025	0.028

density-based solver. The convective term is discretized using a second-order upwind scheme, gradient discretization employs a node-based least squares method, and pressure interpolation is conducted using central differencing for face pressure reconstruction.

### 3.2. Computational domain and mesh setup

**Fig. 5** illustrates the computational domain setup. The domain consists of a static and a rotating computational section connected via interfaces to facilitate data interpolation calculations. The cylindrical far-field radius around the duct is set to  $4D$ , with the inlet positioned  $6D$  from the duct, both assigned as pressure-inlet boundary conditions. The outlet, located  $10D$  from the duct, is designated as a pressure-outlet boundary condition. This arrangement assumes constant inlet total pressure and temperature far from the blades, accommodating both steady and unsteady computations. The study

employs a Poly-Hexcore unstructured mesh created using Fluent Meshing software, featuring a hexagonal surface mesh, poly-prism boundary layer mesh, and hexahedral mesh filling the volume. The mesh is refined at curvature variations at intervals of  $10^\circ$ , with additional refinement zones established around the inflow and wake of the propeller. In the rotating computational domain, the boundary layer  $y^+$  value is approximately 1, with a first layer mesh height of 0.003 mm. In the static computational domain, the boundary layer  $y^+$  value is approximately 4.5, with a first layer mesh height of 0.1 mm.

### 3.3. Mesh independence study

The accuracy of numerical studies is generally contingent on mesh size, and for unsteady calculations, the time step size also impacts accuracy. This study focuses on the Case-1D1P model, assessing the influence of size on mesh independence concerning spatial discretization. By specifying different minimum mesh sizes for the propeller and duct surfaces, the total number of mesh nodes is set at 3.2 million, 6.6 million, 13.2 million, and 16.3 million. **Table 3** demonstrates detailed parameters for the mesh independence study. The variations in thrust and efficiency across iterations for these meshes are depicted in **Fig. 6**. The oscillatory characteristics of the data are a common occurrence for the SMM model.<sup>12,14,18</sup> It is evident that the computed values for both parameters are nearly identical when employing meshes of 13.2 million and 16.3 million nodes. A slight variation is noted at 6.6 million nodes, while a significant error arises when the node count is reduced to 3.2 million. The results suggest that a mesh size of 13.2 million nodes is suitable for unsteady simulations of the ducted propeller, where the minimum mesh size is set to 0.5 times the

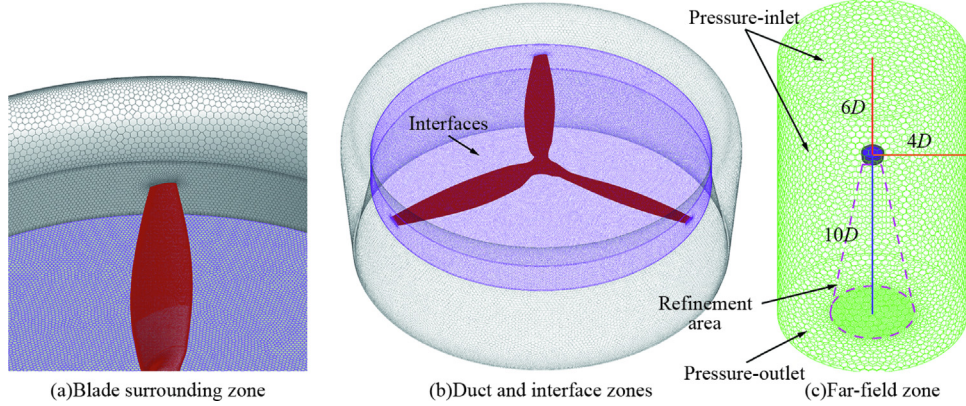


**Fig. 5** Computational domain setup.

**Table 3** Mesh parameters for independence study.

Count ( $10^6$ )	Propeller mesh size (m)	Duct mesh size (m)	Refinement area size (m)
3.2	0.000 4	0.004	0.016–0.064
6.6	0.000 3	0.003	0.016–0.064
13.2	0.000 2	0.002	0.016–0.064
16.3	0.000 2	0.002	0.008–0.032

smallest geometric dimension. This mesh configuration is applied consistently across all cases presented.

The rotation process of the ducted propeller is inherently unsteady, necessitating further consideration of time step independence. This paper evaluates different time step sizes to assess the aerodynamic performance of the ducted propeller based on the spatial discretization independence study. Time steps of  $dt = 0.000\ 1$ ,  $0.000\ 2$ ,  $0.000\ 4$ , and  $0.000\ 8$  s are selected, corresponding to rotations of  $2.4^\circ$ ,  $4.8^\circ$ ,  $9.6^\circ$ , and  $19.2^\circ$ , respectively. The variations in thrust and efficiency across iterations for these time steps are shown in Fig. 7. The results indicate that we can achieve comparable aerodynamic performance with time steps of  $dt = 0.000\ 1$  s and  $dt = 0.000\ 2$  s. In contrast, time steps greater than  $dt = 0.000\ 4$  s lead to significant inaccuracies in the aerodynamic performance. Thus, the time step size in this paper is set to achieve a rotation of  $4.8^\circ$  per time step, satisfying the accuracy requirements for all cases.

Detailed numerical and mesh parameters used in the calculations are provided in Table 4 and Table 5.

### 3.4. Numerical validation

The aerodynamic characterization tests conducted in this paper took place in the FL-5 wind tunnel at the AVIC Aerodynamics Research Institute. Fig. 8 illustrates the configuration of the experimental platform for the ducted propeller model Case-WT. The tests utilized a 19-N6-24C six-component force balance to measure the aerodynamic forces and moments across three axes. Calibration was performed using a self-compensating static calibration setup and a Versa

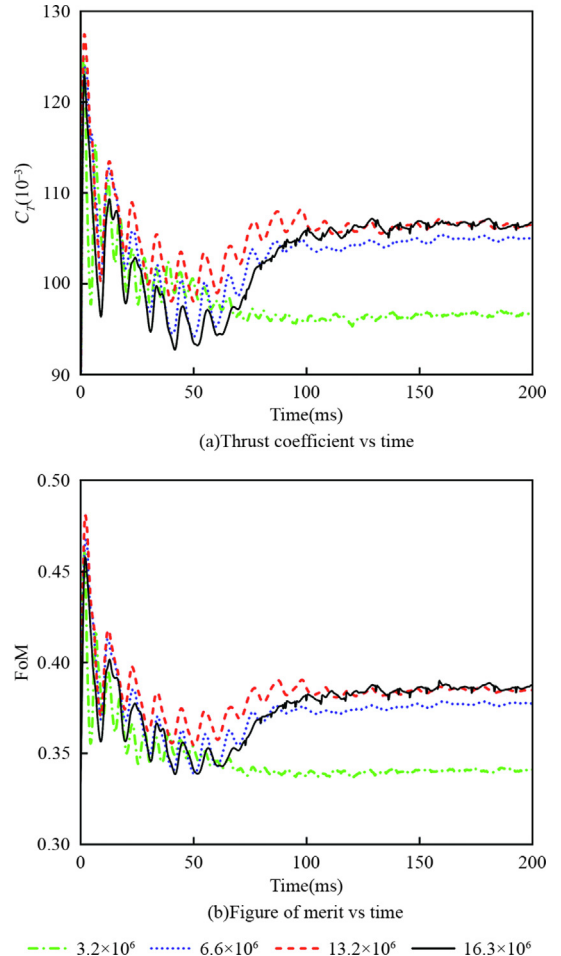


**Fig. 6** Analysis of mesh independence in spatial discretization.

module eurocard eXtensions for Instrumentation (VXI) bus acquisition system, achieving a sampling rate of 100 Kbps. A Hall sensor in the motor monitored the rotational frequency during testing, with an error margin of 1 r/min. We used a DC power supply to power the ducted propeller model, transmitting real-time current data via an RS-485 module. The static side force was oriented perpendicular to the flow direction of the test section to avoid wake acceleration in the wind tun-

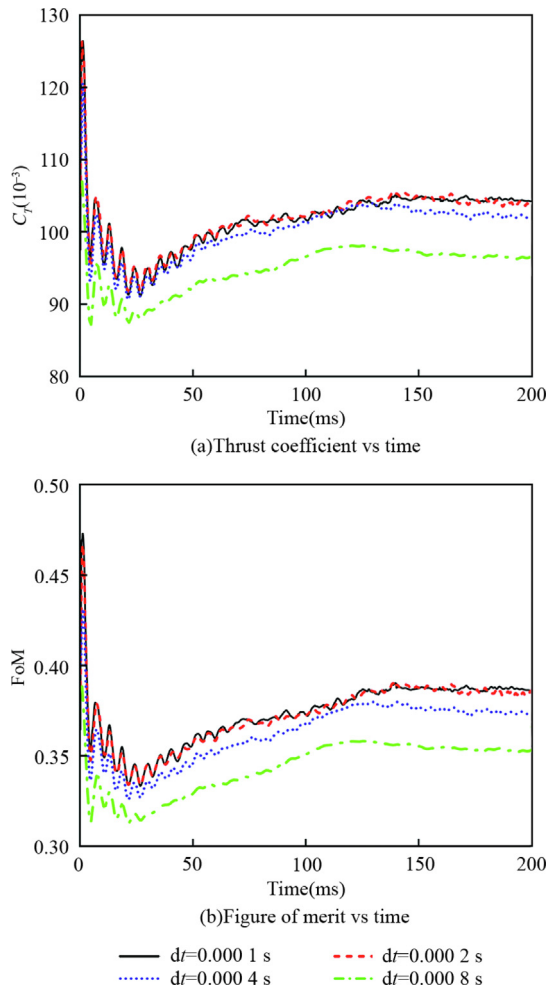


**Fig. 7** Analysis of mesh independence in temporal discretization.

**Table 4** Numerical simulation conditions.

Parameter	Value
Temperature (K)	288
Pressure (Pa)	101 325
Steady-state iterations	1 000
Iterations per timestep	15
Timestep rotation ( $^{\circ}$ )	4.8
Inflow velocity (m/s)	0
Total iterations per rotation (r)	26
Tip Mach number	0.46, 0.51, 0.57, 0.63, 0.69

nel. The mounting structure can be connected to the balance and the motor on both sides to measure the overall force, as shown in Fig. 8(b). Fig. 8(c) demonstrates an alternative configuration where the balance directly attaches to the motor. Concurrently, cylindrical supports secure the mounting structure to the supporting frame, isolating force measurements to those generated solely by the propeller in the duct. This setup facilitates the calculation of forces and moments for each component at consistent rotational frequencies.

The transient URANS numerical simulations of the ducted propeller yield solutions characterized by oscillatory behavior. Time-averaged aerodynamic characteristics over each cycle of the stable oscillatory regime are extracted and employed to evaluate the aerodynamic performance. The thrust and torque values of the propeller within the duct, derived from comparisons of numerical simulations with experimental data, are presented in Fig. 9. In the rotational frequency range of 3 500 r/min to 6 000 r/min (corresponding to a blade tip Mach number range of 0.46 to 0.69), the numerical simulation results are slightly higher than the measured values. The average error in propeller thrust prediction is less than 5%, with a maximum error of 8.9%. For torque, the average error is approximately 10%, with a maximum error of 13.8%. These errors fall within the combined standard uncertainty of the testing equipment. The control surfaces, mounting frame, and landing gear are omitted in the numerical model, which likely contributed to the discrepancies observed between the numerical and experimental results.

#### 4. Results and discussion

A comparative study is performed through numerical simulations to investigate the differences in aerodynamic performance across various equivalent ducted propeller cases under hovering conditions. The aerodynamic performance is evaluated using non-dimensional parameters such as the  $C_T$  and FoM. Among the three cases, Case-1D1P utilizes complete aircraft data for aerodynamic performance evaluation, while Case-1D2P and Case-2D2P are configured as counter-rotating, using half-duct or average data for performance assessment. The relationship between thrust and power for these cases is examined to define the operational characteristics of the equivalent ducted propellers. The aerodynamic performance of the propellers and ducts across different cases, under counter-rotating conditions with identical blade tip Mach number, is analyzed, revealing key aerodynamic trends.

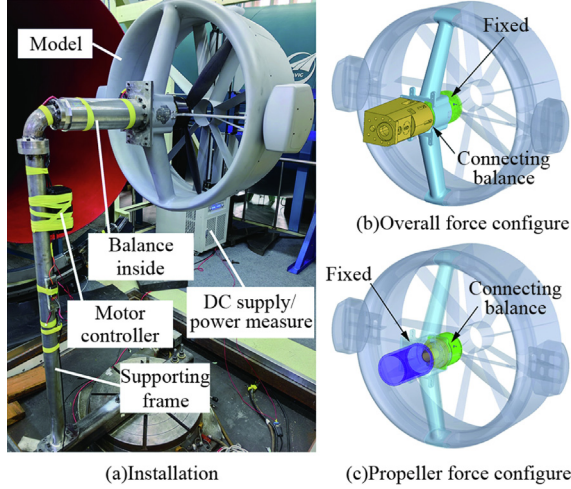
Additionally, the sensitivity of the aerodynamic characteristics to blade tip Mach number and rotational consistency is explored. The  $Ma_{tip}$  range of 0.46 to 0.69 is selected to encompass subsonic to transonic operating conditions. In the study of rotational consistency, Case-1D1P is used as a benchmark to compare the aerodynamic performance of the other cases. Since rotational consistency primarily influences Case-1D2P, a deeper analysis of the flow field mechanisms for this case is conducted. Further investigations into the influence of each aerodynamic parameter and the associated flow field characteristics are carried out in subsequent studies.

##### 4.1. Aerodynamic characteristics of equivalent ducted propeller cases

Initially, this section employs numerical simulations to evaluate the thrust and power of three equivalent ducted propeller cases based on similarity criteria under hovering conditions. Fig. 10 illustrates the relationship between thrust and power. As observed, the thrust-power curves of the three equivalent cases exhibit substantial overlap, which indicates the ability to generate comparable thrust under similar power consumption. The findings align with the initial computational goals, reinforcing the viability of employing equivalent ducted pro-

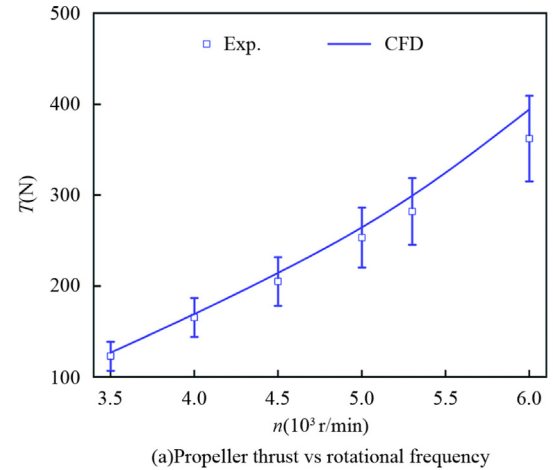
**Table 5** Mesh parameters of three cases.

Case	Count ( $10^6$ )	Propeller size (m)	Duct size (m)	Refinement area size (m)
1D1P	13.2	0.0002	0.002	0.016–0.064
1D2P	25.3	0.00015	0.0014	0.012–0.048
2D2P	19.3	0.00015	0.0014	0.012–0.048

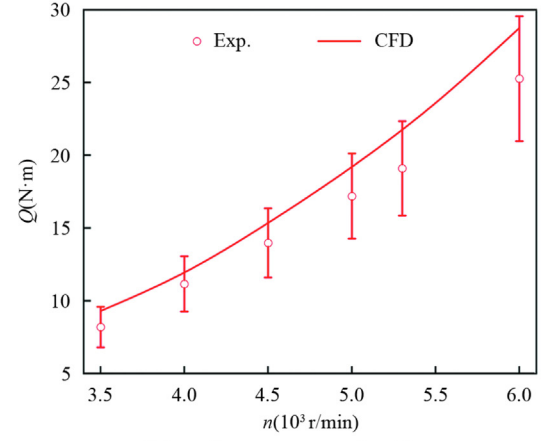
**Fig. 8** Installation of Case-WT and measurement equipment.

peller designs and similarity criteria to establish a unified assessment standard for diverse configurations. Component performance analysis reveals that propeller thrust is highest for Case-1D2P and lowest for Case-1D1P, though overall agreement remains high. Significant differences exist in duct thrust across configurations under identical power consumption, where Case-1D1P exhibits the highest duct thrust, while Case-1D2P shows the lowest across the entire power range.

Under a tip Mach number of 0.57, the pressure distribution characteristics of propellers across different cases are examined. Figs. 11(a), (b), and (c) illustrate the  $C_p$  contour plots derived from computational analyses. The primary differences in pressure distribution among the three cases are noted at the tips, where Case-2D2P exhibits a significantly lower pressure on the suction side than Case-1D1P. In contrast, differences on the pressure side are minimal. Case-1D2P shows lower pressure on the suction side relative to the other two cases, alongside a higher pressure on the pressure side. Notably, Case-1D2P demonstrates pronounced fluctuations in contour lines at the blade root LE. This phenomenon is due to the severe flow interference in Case-1D2P, which causes vortex shedding from the upstream blade's leading edge to affect the downstream blade's leading edge. Fig. 12 shows the Mach number distribution on the isosurface with a vorticity magnitude of 1 000, characterizing the vorticity structures and flow interference in the flow field. Since the blade root is in a region with lower linear velocity at the same rotational speed, it experiences more significant flow interference than the blade tip. The flow interference mechanism is reflected in the pressure distribution, where significant fluctuations occur at the blade root and gradually diminish as  $R^*$  increases.



(a) Propeller thrust vs rotational frequency



(b) Propeller torque vs rotational frequency

**Fig. 9** Comparison of aerodynamic performance between experiment and CFD results for Case-WT.

Fig. 13 examines the pressure distribution characteristics of the propellers' suction and pressure surfaces for the three cases under different tip Mach number. The  $x/c$  value 1 corresponds to the TE, while 0 corresponds to the LE. The pressure distributions of Case-2D2P and Case-1D1P are similar, but Case-2D2P exhibits a higher  $C_p$  on the pressure surface at  $R^* = 0.9$  and a lower  $C_p$  on the suction surface, resulting in a higher  $C_T$  compared to Case-1D1P. In contrast, the  $C_p$  distribution for Case-1D2P shows a notable divergence from the other cases. Radially, this difference is less pronounced in the middle sections of the blade ( $R^* = 0.5$  and  $R^* = 0.7$ ) but more evident at the blade root ( $R^* = 0.3$ ) and tip ( $R^* = 0.9$ ). At the blade root, the lower  $C_p$  on the suction sur-

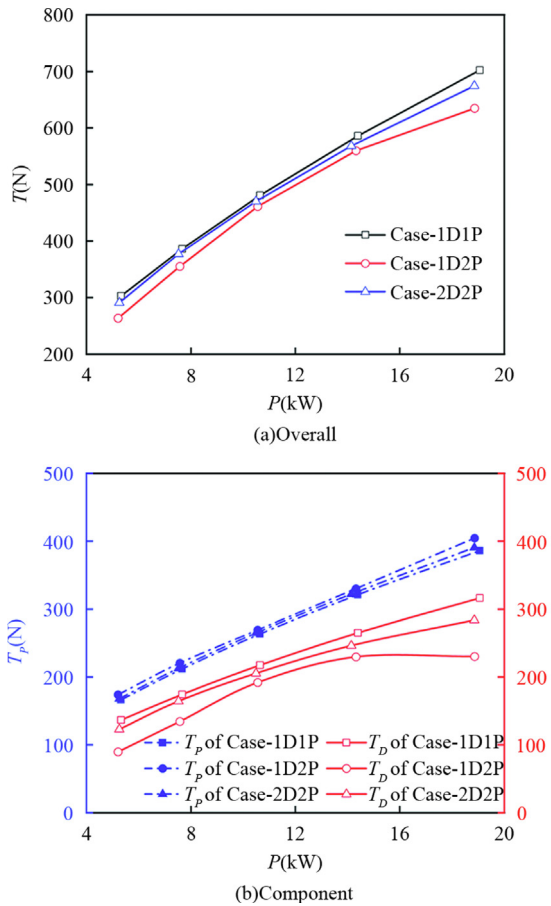


**Fig. 10** Relationship between thrust and power for three equivalent ducted propeller cases.

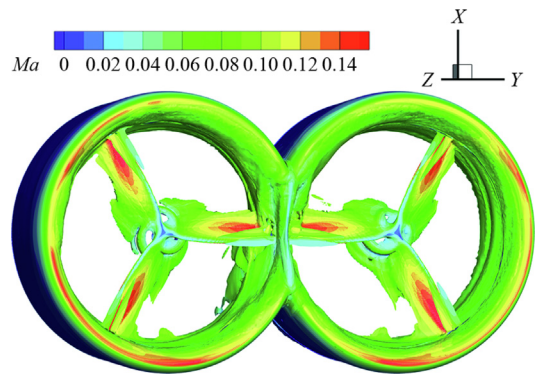


**Fig. 12** Mach number distribution on the isosurface (Vorticity magnitude =  $1000 \text{ s}^{-1}$ ).

face of Case-1D2P contributes more significantly to thrust. However, at the blade tip, the  $C_p$  distribution of Case-1D2P is more influenced by the chordwise position, leading to slightly lower or equal thrust than the other cases.

In a hovering state, duct thrust primarily arises from the LE flow. Under a tip Mach number of 0.57, the pressure distribution characteristics at the LE of the duct across different cases are analyzed. Figs. 14(a), (b), and (c) show the resulting  $C_p$  contour. Case-1D1P serves as the benchmark, highlighting a low-pressure region at the duct LE characterized by a uniform low-pressure area away from the blade tip wake and a very low-pressure zone behind it. In Case-2D2P and Case-1D2P, the sides of the ducts in nearby are termed the crossing side, while the distant sides are termed the non-crossing side. In Case-2D2P, the uniform low-pressure area on the crossing side experiences a slight increase in  $C_p$ , while the very low-pressure area sees a marked increase. The pressure distribution on the

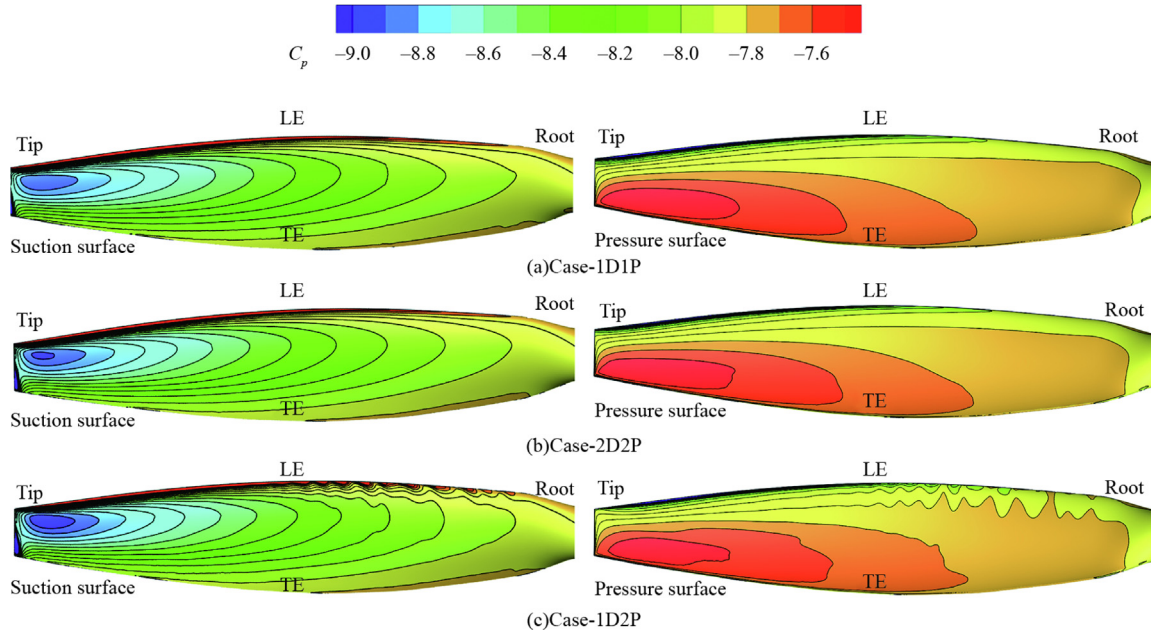


**Fig. 11** Pressure distribution at propeller surfaces ( $\text{Ma}_{\text{tip}} = 0.57$ ).

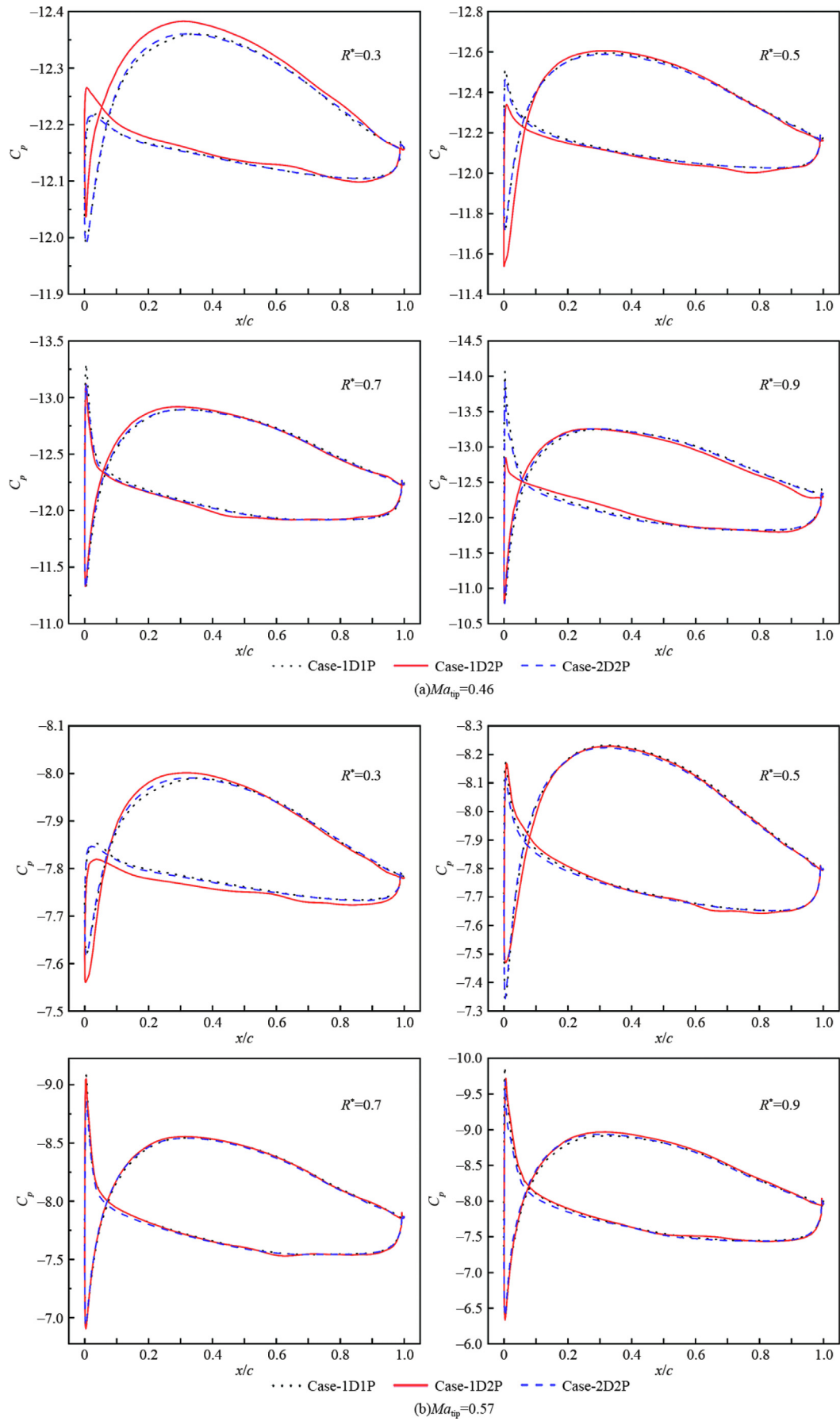


**Fig. 13** Radial pressure coefficient distribution for three cases.

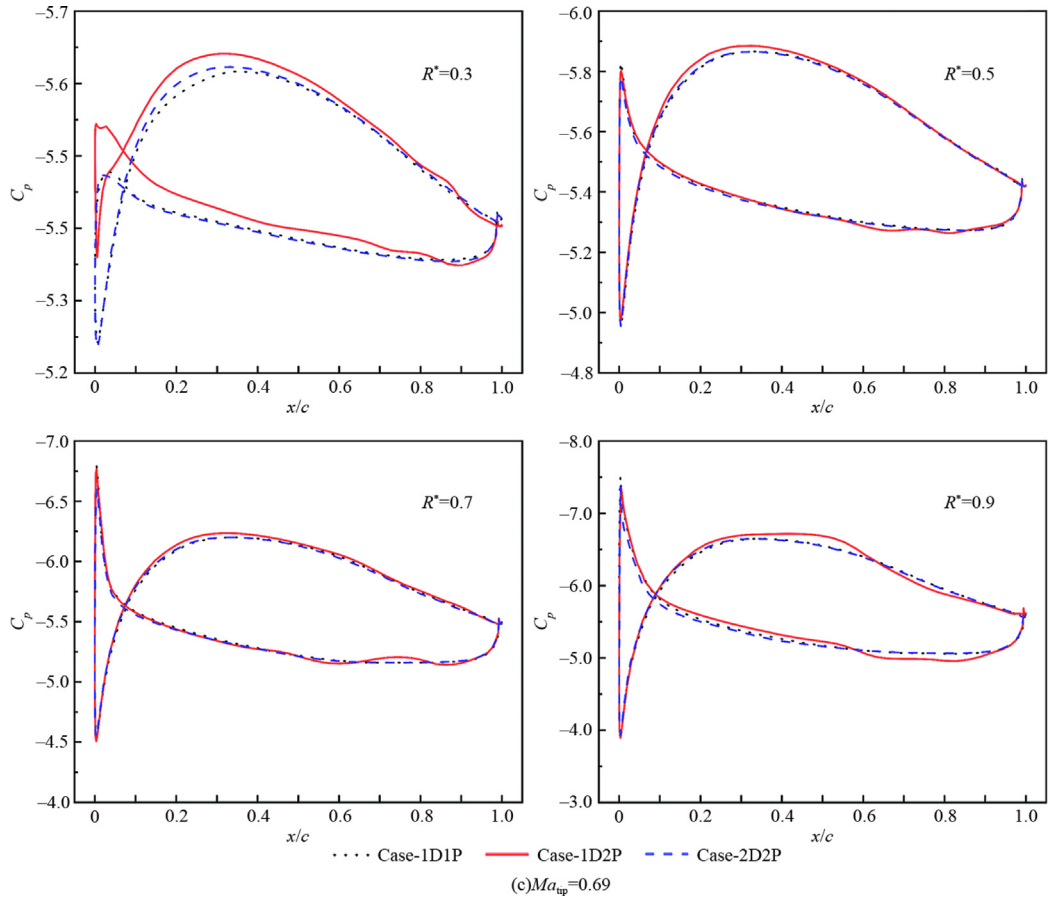
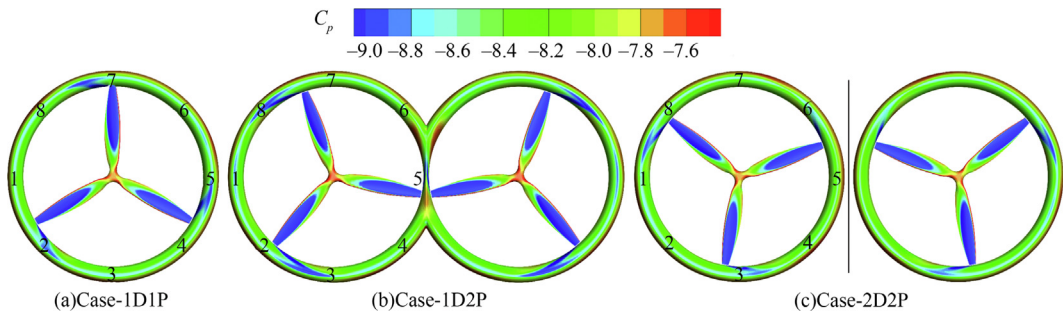


Fig. 13 (continued)

Fig. 14 Pressure distribution at duct LE ( $Ma_{tip} = 0.57$ ).

non-crossing side does not show significant differences compared to the Case-1D1P. In Case-1D2P, the uniform low-pressure area on the crossing side shows a dramatic increase in pressure, with a minor increase in negative pressure in the very low-pressure zone. The non-crossing side also shows minimal changes in pressure distribution. The weighted average of the  $C_p$  at the LE and TE of the duct cross-section is calculated using the propeller position as the boundary, and the comparisons of  $C_p$  at each SP are presented in Fig. 15. It is evident that the  $C_p$  at the TE of the three Cases are similar, while significant differences exist at the LE, underscoring the critical role of LE interference on duct thrust. Case-1D1P has a lower average LE pressure than Case-1D2P and Case-2D2P at most SPs, which accounts for its superior duct thrust among all cases. The pressure distributions in Case-2D2P and Case-

1D1P are relatively close. However, the LE pressure on the non-crossing side of Case-1D2P is slightly higher than that of Case-2D2P, but the LE pressure on the crossing side (SP 5) rises sharply while the TE pressure decreases rapidly, resulting in a lack of thrust. This is the main reason that Case-1D2P exhibits the lowest duct pressure.

#### 4.2. Effect of tip Mach number on aerodynamic performance of equivalent cases

Fig. 16(a) illustrates the comparative overall  $C_T$  of the three cases as the tip Mach number ranges from 0.46 to 0.69. Case-1D1P consistently achieves the highest  $C_T$  at identical tip Mach number, while Case-1D2P records the lowest. As

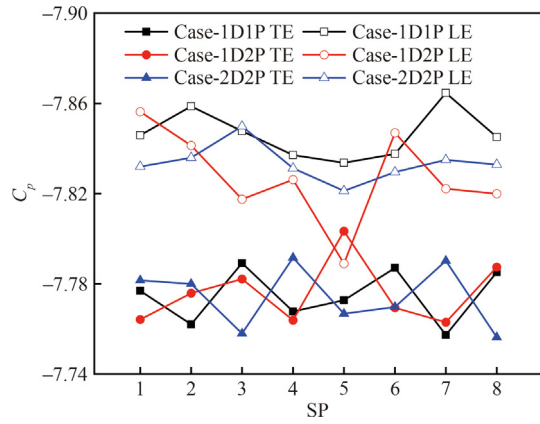


**Fig. 15** Comparison of average pressure coefficient at duct LE and TE for three cases.

the tip Mach number progresses from 0.46 to 0.69, the  $C_T$  of Case-1D1P demonstrates a steady increase from 0.177 to 0.182. In contrast, the  $C_T$  of Case-2D2P initially rises from

0.172 to 0.179 before a slight decline, and the  $C_T$  of Case-1D2P experiences a notable increase from 0.155 to 0.174, followed by a significant drop. Both Case-1D2P and Case-2D2P reach their peak  $C_T$  around a tip Mach number of 0.62, attributable to the proximity of the two propellers, which engenders both propeller-propeller and propeller-duct interference, thus impacting the duct vortex suppression capabilities and the additional thrust at the duct LE. The intensity of this interference varies with the tip Mach number, delineating an optimal range for aerodynamic performance.

**Fig. 16(b)** depicts the relationship between the component  $C_T$  and tip Mach number for the three cases. With increasing tip Mach number, propeller  $C_T$  rises monotonically, with Case-1D2P showing the highest propeller  $C_T$  and Case-1D1P the lowest. This trend contrasts with the overall  $C_T$  of the three Cases. This observation aligns with the phenomenon presented in **Fig. 13**, where the differences in blade  $C_p$  at three different tip Mach number are noticeable but insignificant. However, the trend for the duct  $C_T$  mirrors that of the overall  $C_T$ . The reduced sensitivity of propeller-propeller interference on  $C_T$  concerning tip Mach number enables a modest enhancement

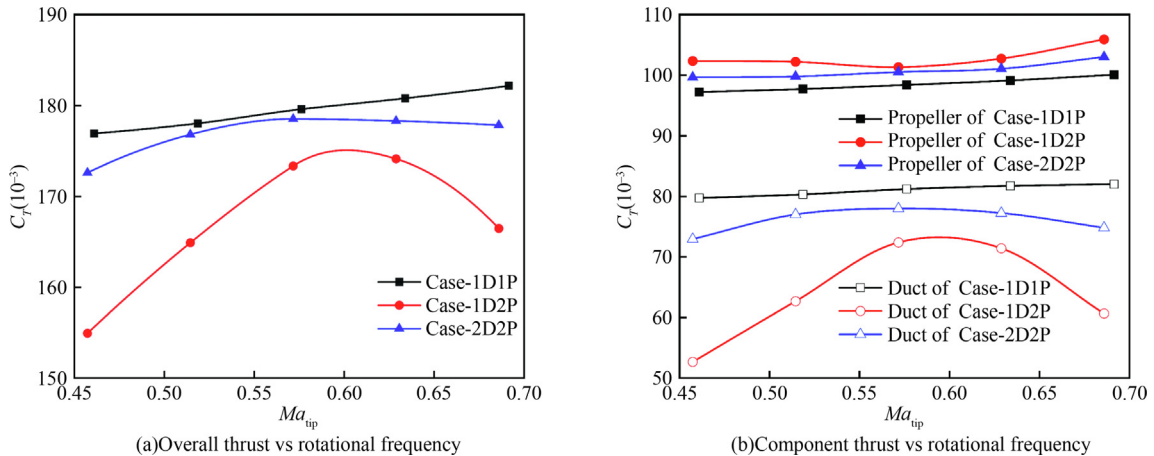


**Fig. 16** Comparison of thrust coefficient for three cases.

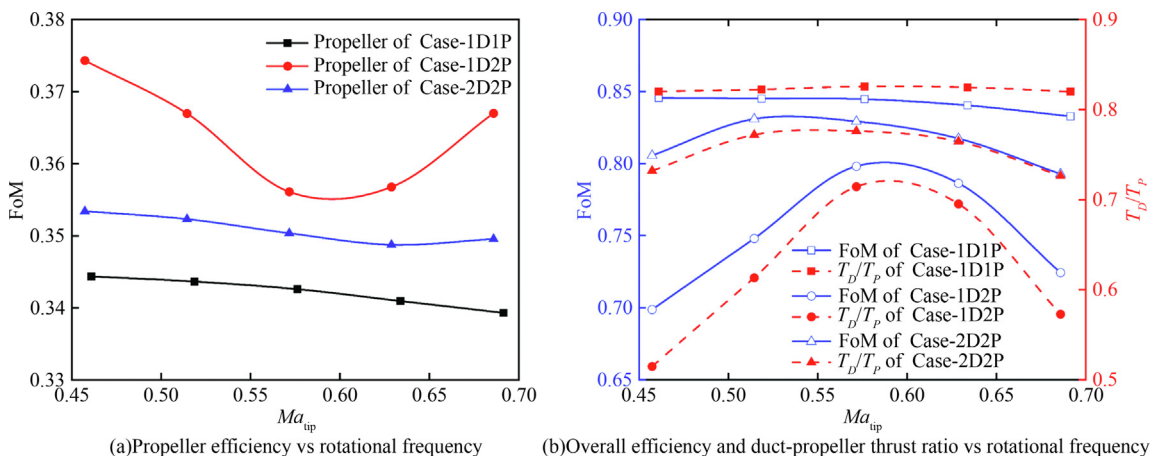


**Fig. 17** Efficiency evaluation for three cases.

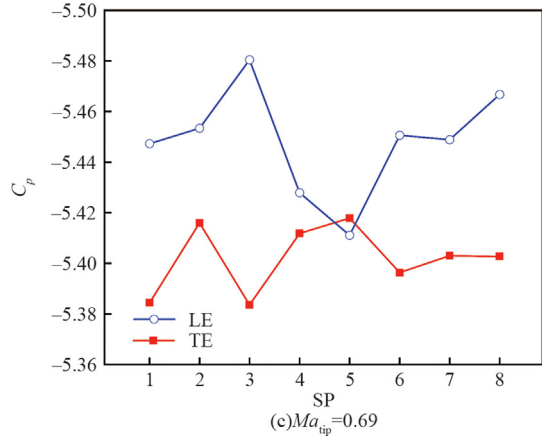
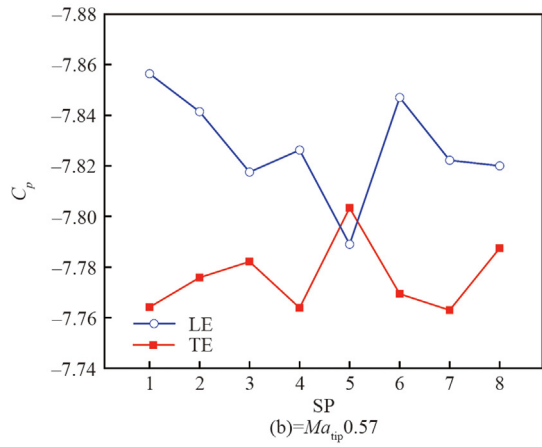
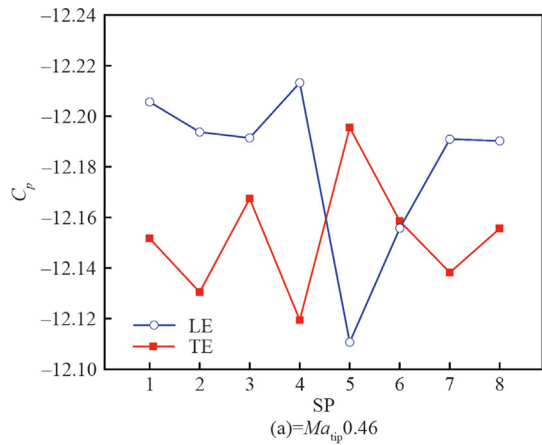


**Fig. 18** Average pressure distribution at duct LE and TE for Case-1D2P.

of propeller  $C_T$ . Conversely, propeller-duct interference significantly affects the sensitivity of duct  $C_T$  to tip Mach number, reducing duct  $C_T$ .

In propeller aerodynamics, FoM is usually employed to signify hovering efficiency.<sup>28</sup> Fig. 17(a) illustrates the correlation between the propeller FoM for the three cases and the tip Mach number. The trends for Case-1D1P and Case-1D2P indicate that absent interference, propeller efficiency declines monotonically with rising tip Mach number. For Case-1D2P,

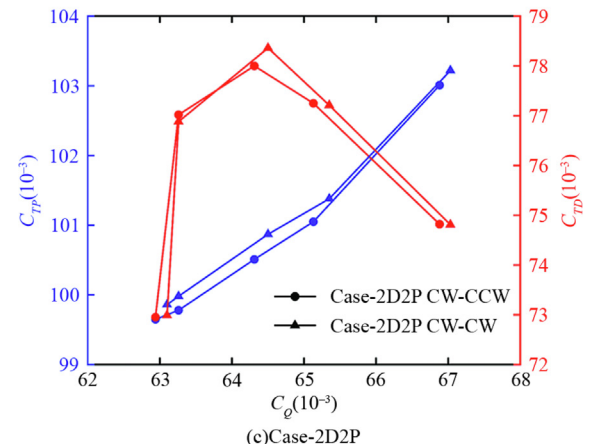
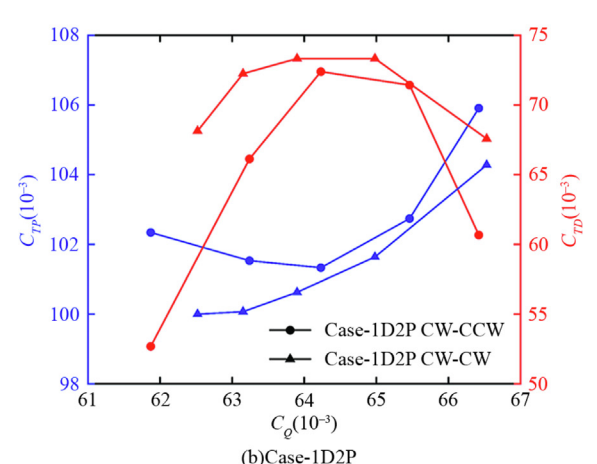
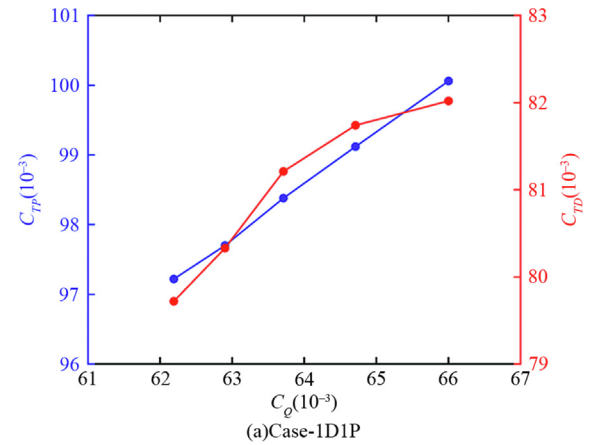


**Fig. 19** Comparison of propeller and duct thrust coefficients vs power coefficients under different rotational consistency.

the propeller efficiency exhibits an initial decrease followed by an increase in tip Mach number, consistently outperforming the other two cases across varying tip Mach number. This further reinforces the notion that propeller-propeller interference enhances propeller thrust. Fig. 17(b) contrasts the thrust ratio between the duct and the propeller against the overall quality factor as the tip Mach number fluctuates from 0.46 to 0.69 for the three cases. Notably, while the magnitudes of the two ratios differ across various cases, especially in Case-1D2P,

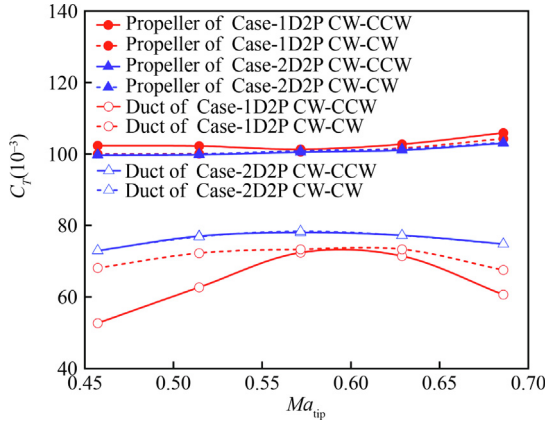


**Fig. 20** Component thrust coefficients of two cases under different rotational consistency.

their overall trends align. When torque or power data is unavailable, the thrust ratio between the duct and propeller can serve as a reliable estimate of the hovering efficiency for comparable cases.

As the tip Mach number varies from 0.46 to 0.69, the average  $C_p$  at various SPs along the duct for Case-1D2P are shown in Fig. 18, which allows for a quantitative analysis of how aerodynamic interference influences the LE-TE pressure differential at different rotational frequencies, impacting the duct thrust. At a tip Mach number of 0.46, the  $C_p$  difference between the non-crossing side LE and TE is minimal, while the pressure at the crossing side TE is markedly lower, reducing duct thrust. At a tip Mach number of 0.57, the difference in average  $C_p$  at the non-crossing side edges increases, with an elevated TE  $C_p$  on the crossing side and a decreased LE  $C_p$ , which increases duct thrust. As the tip Mach number rises to 0.69, the  $C_p$  distributions for both sides closely resemble those at 0.57, reflecting only slight variations in duct thrust. This observation clarifies the trends in duct thrust changes for Case-1D2P depicted in Fig. 10.

#### 4.3. Impact of rotational consistency on aerodynamic performance of Case-1D2P

Experimental findings indicate that rotational consistency significantly affects the propeller slipstream in distributed propeller systems.<sup>25</sup> Investigating its role in distributed ducted propellers is valuable. This study initially examines the sensitivity of different cases to rotational consistency. Fig. 19 illustrates the relationships between  $C_T$  and power coefficient ( $C_Q$ ) for the three cases under different rotational consistency. Serving as a reference, Case-1D1P features a single rotation direction. As  $C_Q$  increases, the propeller  $C_T$  of Case-1D1P increases linearly and monotonically, while the duct  $C_T$  increases monotonically but with a decelerating rise. In Cases-2D2P and Cases-1D2P, the rotation direction of one propeller is adjusted without changing the initial phase angle. The co-rotating case is Clockwise-Clockwise (CW-CW), and the counter-rotating case is Clockwise-Counterclockwise (CW-CCW). For Case-1D2P, the  $C_T$ - $C_Q$  curves under different rotational consistency do not overlap. With increasing  $C_Q$ , the blade  $C_T$  in Case-1D2P CW-CW increases monotonically with an accelerating

slope, whereas in Case-1D2P CW-CCW, the propeller  $C_T$  initially decreases slightly before growing substantially. The duct  $C_T$  in both cases first increases and then decreases, but the extent of variation differs. In Case-2D2P, the  $C_T$ - $C_Q$  curves coincide under different rotational consistency. While the propeller  $C_T$  mirrors that of the reference, the duct  $C_T$  exhibits significant differences, initially increasing and then decreasing. Fig. 20 presents the relationships between component  $C_T$  and tip Mach number for Case-2D2P and Case-1D2P under different rotational consistency. The aerodynamic performance of components in Case-2D2P remains consistent, whereas significant disparities are observed in Case-1D2P, especially at low tip Mach number. The  $C_T$  loss in Case-1D2P is primarily attributed to the duct rather than the propeller. These findings suggest that Case-2D2P is insensitive to rotational consistency, whereas Case-1D2P is sensitive, with effects mainly evident at low tip Mach number. Future research will delve into the flow field characteristics based on Case-1D2P.

Fig. 21 illustrates the oscillatory behavior of the aerodynamic performance for Case-1D2P under different rotational consistency at  $Ma_{tip} = 0.46$ . In the negative y-axis region of the half-duct, the initial SP is set to 7. The SPs are sequentially set to 7, 5, 3, and 1 to evaluate the characteristics of each blade passing through both the crossing and non-crossing sides. Consequently, a full rotation of the three-blade propeller requires the analysis of 12 data sets, with aerodynamic characteristics assessed every  $30^\circ$  of rotation. Each parameter undergoes an entire cycle every  $120^\circ$ , i.e., after every four data sets. During each cycle, the 2nd and 4th points correspond to the blade passing through the non-crossing and crossing sides (i.e., SPs 1 and 5). It is evident that all parameters oscillate within a convergent range, but the amplitude of oscillation for Case-1D2P CW-CW is significantly smaller than for Case-1D2P CW-CCW.

The duct thrust for Case-1D2P CW-CCW also oscillates in the output values and exhibits oscillatory features in its median value. This behavior is not observed for other parameters, suggesting that in Case-1D2P, disturbances caused by non-consistent rotation have a more significant effect on the duct itself. This indicates that Case-1D2P CW-CCW requires more iterative time steps than any other case, i.e., a more extended rotation period after startup to achieve a relatively stable oscillatory state. Within each cycle, blade thrust and torque in Case-1D2P CW-CCW are highest when the blade passes through the crossing side (the 4th point) and lowest when passing through the non-crossing side (the 2nd point). In Case-1D2P CW-CW, blade torque is highest when the blade passes through the crossing side, with other oscillatory characteristics of aerodynamic performance similar to those observed in Case-1D2P CW-CCW, though not at the extremes. It suggests that aerodynamic interference between ducts enhances both blade thrust and torque, though the points at which the extremes occur vary depending on the rotational consistency. Furthermore, the duct thrust oscillation characteristics show significant differences between cases with different rotational consistency, highlighting the considerable impact of aerodynamic interference on the duct.

The pressure distribution characteristics for the suction and pressure surfaces of the propeller in Case-1D2P, under various tip Mach number and rotational consistency, are presented in Fig. 22. Significant differences in the  $C_p$  distribution are

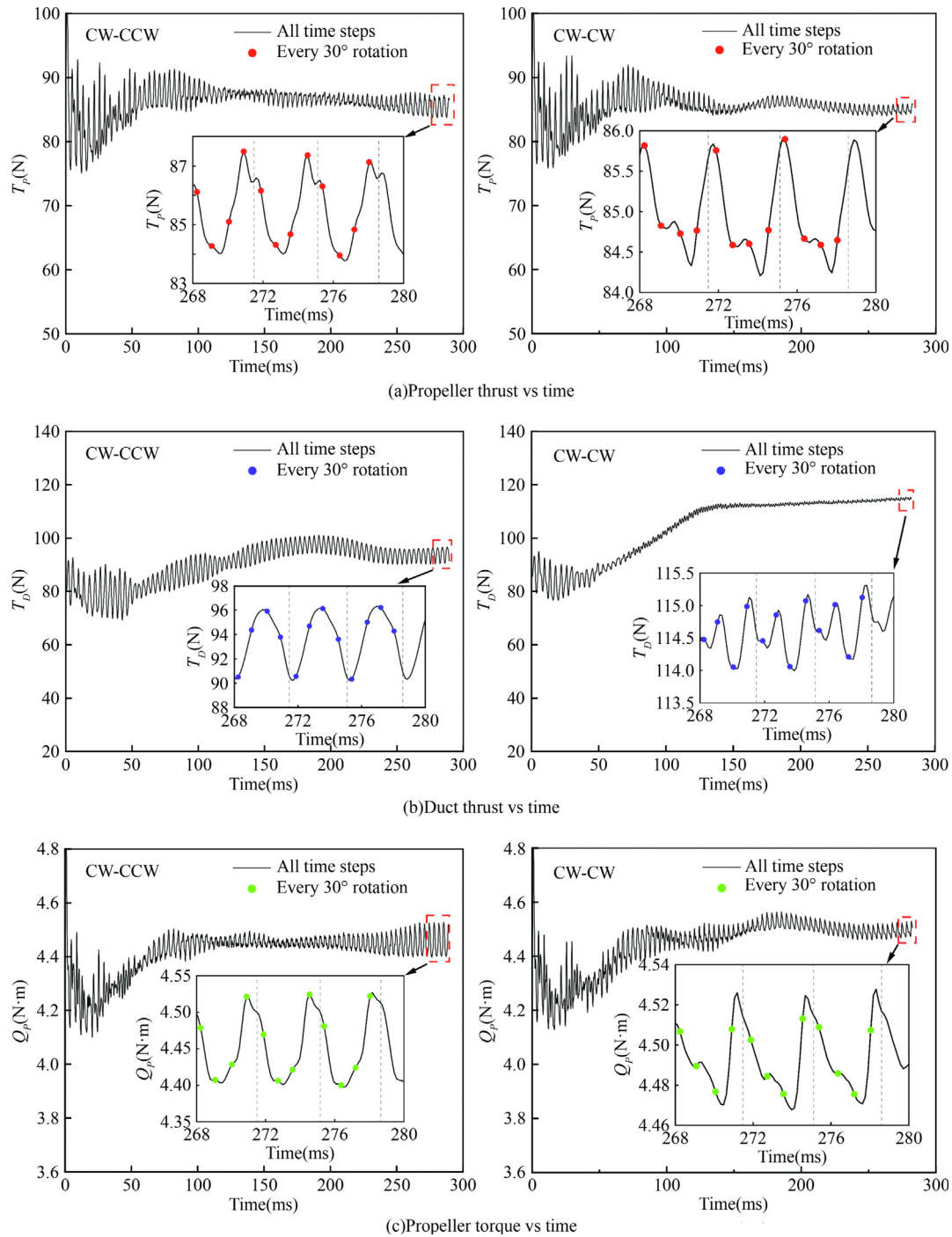


**Fig. 21** Aerodynamic performance oscillatory characteristics for Case-1D2P.

observed for Case-1D2P under different rotational consistency, primarily at the blade root ( $R^* = 0.3$ ) and tip ( $R^* = 0.9$ ), as opposed to the middle of the blade ( $R^* = 0.5$  and  $R^* = 0.7$ ). This behavior is similar to the pressure distribution differences found in other cases. Furthermore, these differences are more pronounced at lower Mach number and less evident at medium to high Mach number.

The differences in pressure characteristics are primarily attributed to variations in airflow velocity. This study analyzes the flow field's airspeed variations at low tip Mach number. Fig. 23 compares the Ma distribution at the central section

during the rotation of Case-1D2P under different rotational consistency at  $Ma_{tip} = 0.46$ . The four data sets correspond to four points in a single cycle, as shown in Fig. 21, where the blades pass through SPs 7, 5, 3, and 1 in sequence. It is evident that, under different rotational consistency, a distinct velocity difference is observed on the non-crossing side of the duct (SP 1), whereas the velocity difference on the crossing side (SP 5) is much smaller. The red square boxes in the figure mark the regions of significant velocity differences. According to Bernoulli's principle, this velocity gradient difference propagates to the pressure distribution at the duct LE, which in

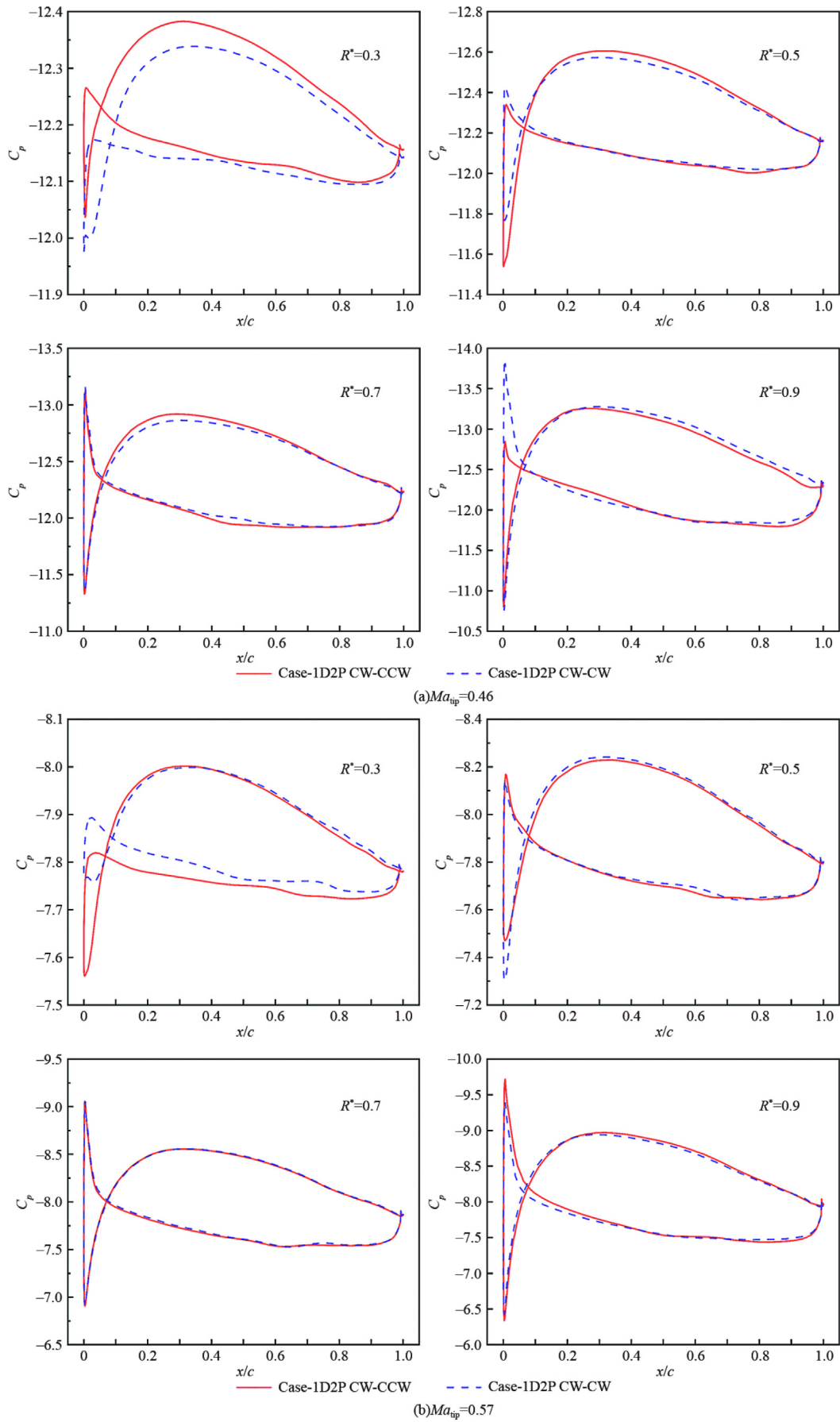


**Fig. 22** Radial pressure coefficient distribution for Case-1D2P under different rotational consistency.

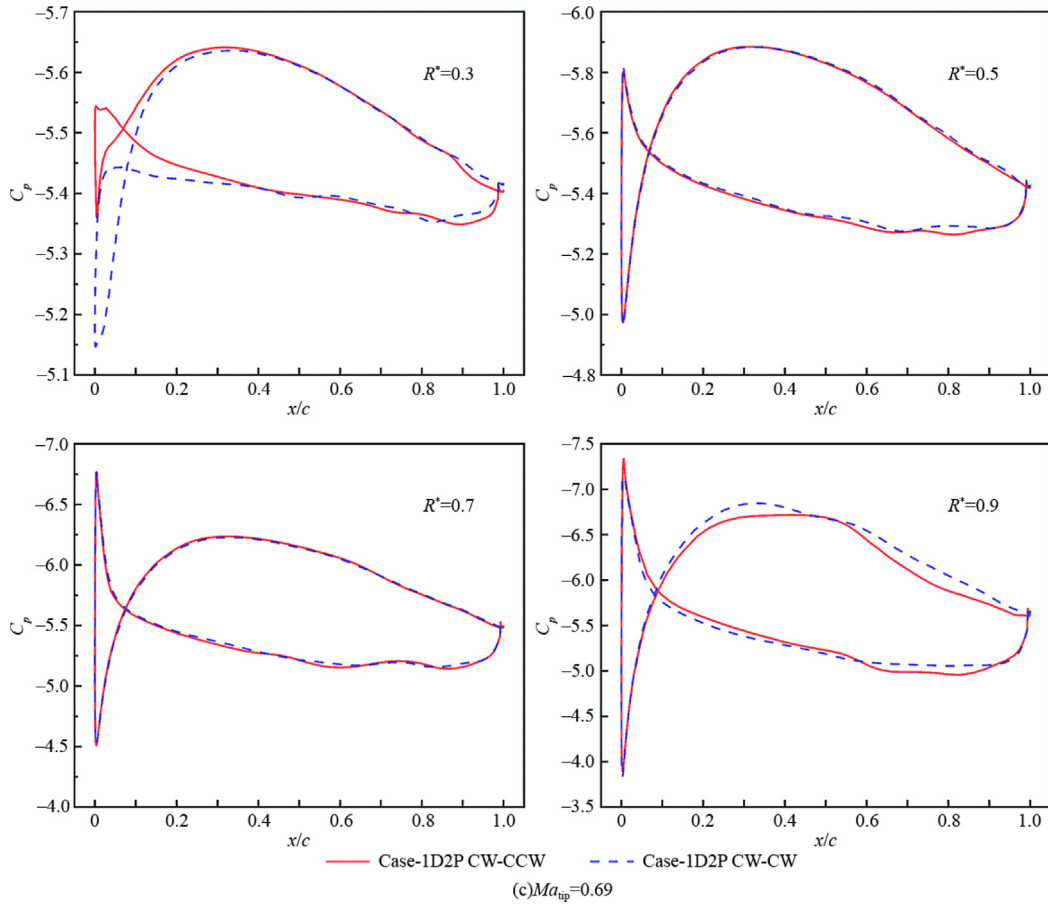


Fig. 22 (continued)

turn causes differences in duct thrust for Case-1D2P. Notably, the velocity gradient at the blade tip is much larger than at the blade midsection or root. The blue circles in the figure highlight the areas with the most apparent velocity gradient. However, in contrast to the duct, for the propeller, the velocity gradient needs to account for the combined effect of the incoming flow velocity and the rotational velocity. As a result, the tip experiences a more significant incoming flow velocity gradient, while the root experiences a smaller linear velocity, leading to considerable pressure distribution differences. This is consistent with the radial  $C_p$  distribution shown in Fig. 22. At the low-speed condition of  $Ma_{tip} = 0.46$ , the combined velocity at the tip, resulting from the incoming flow velocity and lower circumferential velocity, causes a significant difference in the resultant velocity and the angle of attack of blade element. This velocity distribution difference leads to notable pressure differences, ultimately altering the aerodynamic performance. This mechanism of velocity gradient differences explains why the effect of rotational consistency is more pronounced on the aerodynamic characteristics of Case-1D2P at low tip Mach number. As the tip Mach number increases, although the velocity gradient difference persists, the increased linear velocity eventually dominates the resultant velocity, and the influence of rotational consistency diminishes relative to the low tip Mach number case.

The aerodynamic interference generated by varying rotational consistency significantly impacts the ducted propeller's

performance, and analyzing the flow field characteristics is essential for understanding this effect. Figs. 24(a) and (b) illustrate the evolution of vortex structures over a single rotation cycle of Case-1D2P under different rotational consistency, with vorticity depicted at the  $X$ -plane interception position of the duct center. Throughout the flow development, the duct separation vortex, hub separation vortex, and blade wake interact synergistically, while the duct constraints subdue the tip leakage vortex. The flow field is categorized into five regions based on vortex coupling methods, with slight variations in region sizes across different rotational consistencies. Wake generated in Region 2 dissipate and quickly merge into the high-intensity duct separation vortex in Region 1 under centrifugal forces. Conversely, wake in Region 4 dissipate slowly, entering Region 5, where they interact with the low-intensity duct separation vortex, resulting in oscillations. Upon entering Region 3, the wake vortex combine with the hub separation vortex and gradually dissipate. The figures demonstrate that each  $120^\circ$  rotation cycle corresponds to one cycle of propeller wake, with performance oscillations in Fig. 20 showing consistent patterns.

A comparison between Figs. 24(a) and (b) reveals that rotational consistency minimally impacts vortex structures within Regions 1, 2, 3, and 4. However, the vortex development in Region 5 significantly differs with varying rotational consistency. In Case-1D2P CW-CCW, a large-area, low-intensity coupled region forms, rapidly dissipating into a small-scale,

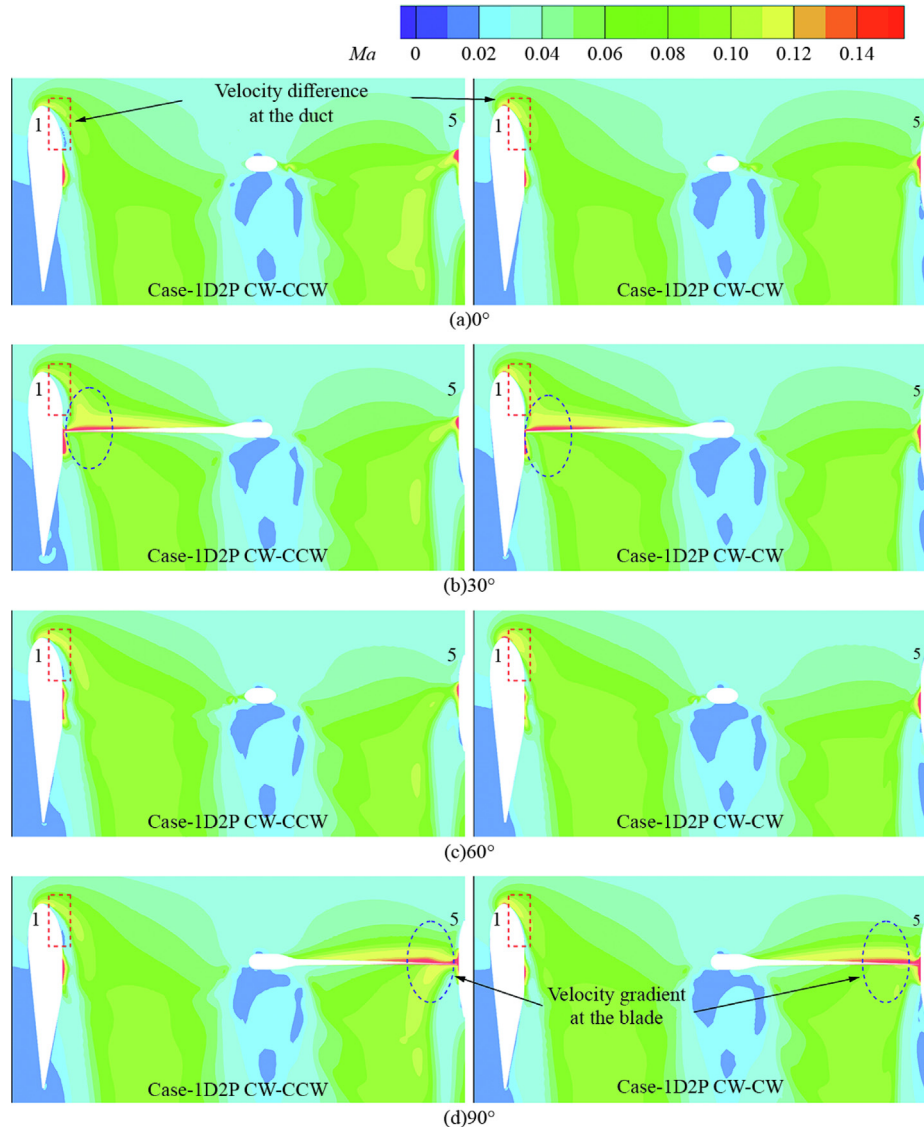


**Fig. 23** Comparison of Mach number distributions for Case-1D2P under different rotational consistency.

asymmetrical, and slowly oscillating structure after detaching from the duct wall. Inconsistent rotation leads to widespread, weak local vortices, resulting in larger boundary layer separation areas and instability of separation vortices. This instability causes rapid energy dissipation, preventing the maintenance of stable vortex structures and leading to large-scale oscillations. Consequently, duct thrust experiences loss and instability, characterized by broad and multi-dimensional oscillations. In contrast, Case-1D2P CW-CW generates a smaller-area, high-intensity coupled region with minimal dissipation post-detachment, forming a large-scale, symmetrical, and rapidly oscillating structure. The oscillation period aligns closely with the propeller rotation period, as illustrated by comparing the 0° and 330° views in Fig. 24(b). Consistent rotation produces concentrated, small-scale vortices near the duct wall in Region 5, reducing flow separation. The slowly dissipating vortices establish a steady-state oscillation structure, promoting flow field stability. This results in lower duct lift loss and reduced oscillation range. The consistent rotation in Case-1D2P optimizes the distribution of vortex structure along the crossing side walls, enhances flow adhesion, and mitigates the dissipation of separated wake, improving overall lift performance.

maximizes the distribution of vortex structure along the crossing side walls, enhances flow adhesion, and mitigates the dissipation of separated wake, improving overall lift performance.

## 5. Conclusions

This study explores the equivalent calculation methods, aerodynamic performance, and flow mechanisms of different distributed ducted propellers, categorized by the number of components. The influence of tip Mach number and rotational consistency on the hovering performance of ducted propellers is assessed. The study also investigates how the velocity–pressure gradient difference in the incoming flow affects blade thrust. The evolution of the flow field in the vortex structure behind the crossing side is analyzed. The main findings are summarized as follows:

An equivalent ducted propeller design method is proposed using the momentum theorem and similarity criteria. Three ducted propeller cases are designed to generate similar thrust

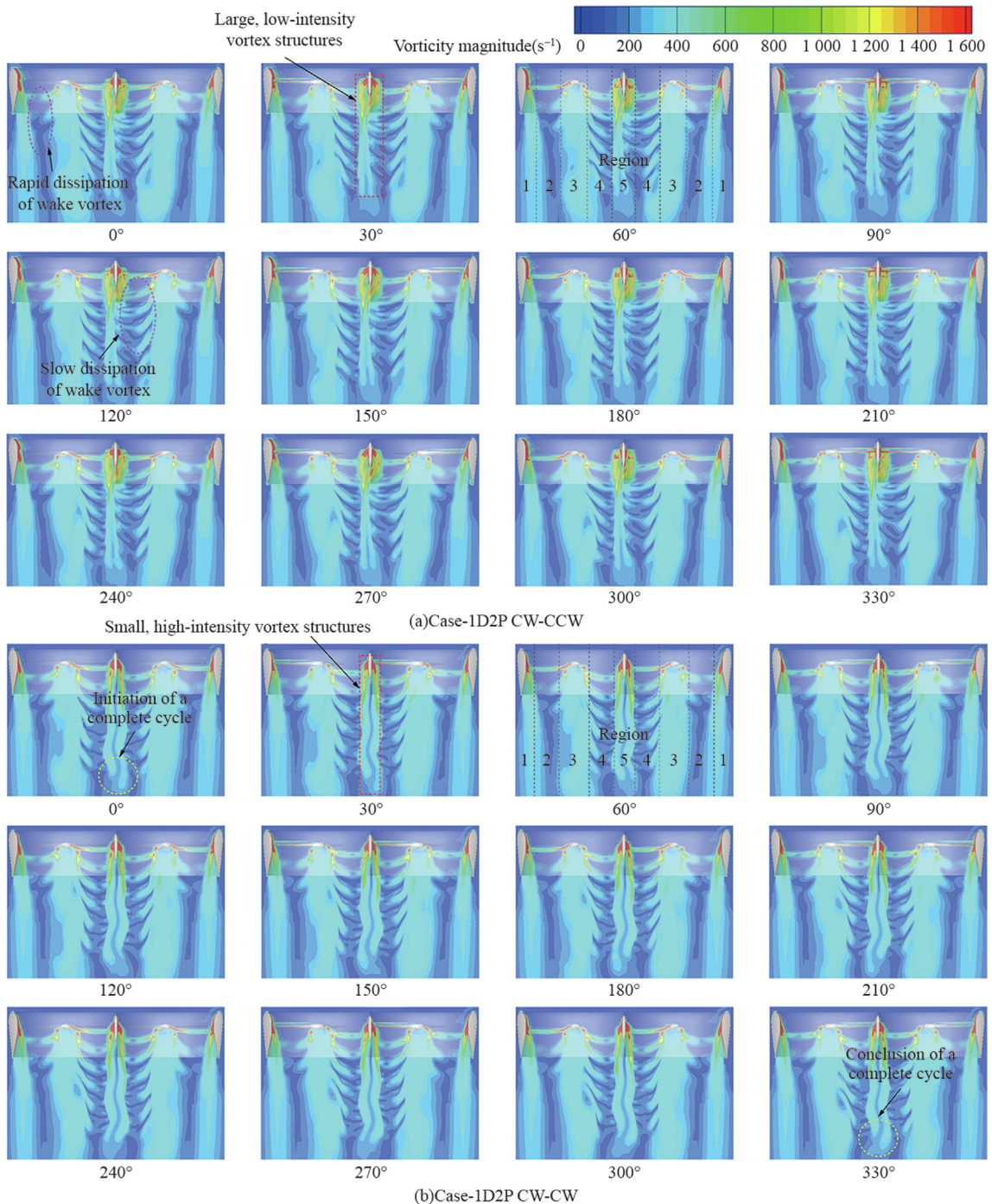


**Fig. 24** Evolution of vortex structures over a single rotation cycle.

at the same power output. Case-1D1P exhibits the most giant-shaped envelope and solid volumes at equivalent power levels, generating the highest duct thrust. In contrast, Case-1D2P reduces the shaped envelope and solid volumes by 32% and 35%, respectively, but results in the lowest duct thrust. Case-2D2P shows a 29% reduction in both volumes, with aerodynamic performance lying between the other two cases. Rotational consistency significantly affects the aerodynamic

performance of Case-1D2P, especially under low-speed conditions, while its influence on Case-2D2P is minimal.

The effect of the tip Mach number on aerodynamic performance is most evident in the variation of duct thrust. At low tip Mach number, the average pressure difference between the LE and expansion section is slight, and the negative thrust at the crossing side is relatively large. At mid-speed conditions, the pressure difference increases, and the negative thrust at the

crossing side decreases rapidly, leading to a sharp rise in duct-induced thrust. In high-speed conditions, the pressure difference stabilizes, and the negative thrust at the crossing side decreases slightly, contributing to a gradual increase in duct-induced thrust.

Rotational consistency has a minor effect on the 2D2P case but significantly influences the aerodynamic characteristics of the 1D2P case. Non-consistent rotation creates significant velocity gradients, which cause differences in the angle of attack at the blade tip, reducing duct thrust but increasing propeller thrust. On the other hand, consistent rotation optimizes vortex shedding on the crossing side surfaces and mitigates flow separation and wake dissipation, resulting in improved overall thrust performance.

#### CRediT authorship contribution statement

**Zeyu LI:** Writing – original draft, Visualization, Validation, Methodology, Investigation, Formal analysis, Data curation, Conceptualization. **Jianghao WU:** Writing – review & editing, Resources, Formal analysis, Conceptualization. **Bairui PEI:** Visualization, Project administration, Data curation. **Long CHEN:** Writing – review & editing, Formal analysis. **Zhengping ZOU:** Supervision, Resources. **Haiying LIN:** Supervision, Resources, Project administration, Funding acquisition.

#### Declaration of competing interest

The authors declare that they have no known competing financial interests or personal relationships that could have appeared to influence the work reported in this paper.

#### Acknowledgements

This study was supported by the Research Funding of Hangzhou International Innovation Institute of Beihang University, China (No. 2024KQ143).

#### References

1. Hildemann M, Versteegen JA. 3D-flight route optimization for air-taxis in urban areas with Evolutionary Algorithms and GIS. *J Air Transp Manag* 2023;107:102356.
2. Zhang T, Barakos GN. High-fidelity numerical analysis and optimisation of ducted propeller aerodynamics and acoustics. *Aerosp Sci Technol* 2021;113:106708.
3. O'Neill S. Electric air taxis create megadeal buzz. *Engineering* 2022;13:5–8.
4. Zhang T, Barakos GN. Review on ducted fans for compound rotorcraft. *Aeronaut J* 2020;124(1277):941–74.
5. Xue C, Zhou Z. Propeller-wing coupled aerodynamic design based on desired propeller slipstream. *Aerosp Sci Technol* 2020;97:105556.
6. Biava M, Barakos GN. Optimisation of ducted propellers for hybrid air vehicles using high-fidelity CFD. *Aeronaut J* 2016;120 (1232):1632–57.
7. Li L, Huang GP, Chen J. Aerodynamic characteristics of a tip-jet fan with a large blade pitch angle. *Aerosp Sci Technol* 2019;91:49–58.
8. Li L, Huang GP, Chen J. Investigations of tip-jet and exhaust jet development in a ducted fan. *Chin J Aeronaut* 2019;32 (11):2443–54.
9. Chen J, Li L, Huang GP, et al. Numerical investigations of ducted fan aerodynamic performance with tip-jet. *Aerosp Sci Technol* 2018;78:510–21.
10. Cao CK, Zhao GQ, Zhao QJ, et al. Numerical investigation and optimization for interior duct shape of ducted tail rotor. *Aerosp Sci Technol* 2021;115:106778.
11. Luo YW, Ai TF, He YH, et al. Aerodynamic analysis on unsteady characteristics of a ducted fan hovering in ceiling effect. *Eng Appl Comput Fluid Mech* 2023;17(1):2196327.
12. Luo YW, Ai TF, He YH, et al. Numerical analysis of wind effects on aerodynamic characteristics of a ducted fan. *Chin J Aeronaut* 2024;37(5):263–80.
13. Luo YW, Ai TF, He YH, et al. Numerical investigation on unsteady characteristics of ducted fans in ground effect. *Chin J Aeronaut* 2023;36(9):79–95.
14. Luo YW, He YH, Ai TF, et al. Numerical study on dynamic performance of a ducted fan moving in proximity to ground and ceiling. *Phys Fluids* 2024;36(11):115151.
15. Zhao YX, Tian Y, Wan ZQ. Aerodynamic characteristics of a ducted fan hovering and transition in ground effect. *Aerospace* 2022;9(10):572.
16. Hu Y, Qing JX, Liu ZH, et al. Hovering efficiency optimization of the ducted propeller with weight penalty taken into account. *Aerosp Sci Technol* 2021;117:106937.
17. Hu Y, Zhang XC, Wang GQ, et al. Hovering efficiency optimization of ducted propeller with large blade tip clearance based on grooved duct configuration. *Aerosp Sci Technol* 2024;150:109226.
18. Mi BG. Numerical investigation on aerodynamic performance of a ducted fan under interferences from the ground, static water and dynamic waves. *Aerosp Sci Technol* 2020;100:105821.
19. Zhang T, Qiao G, Smith DA, et al. Parametric study of aerodynamic performance of equivalent ducted/un-ducted rotors. *Aerosp Sci Technol* 2021;117:106984.
20. Gohardani AS. A synergistic glance at the prospects of distributed propulsion technology and the electric aircraft concept for future unmanned air vehicles and commercial/military aviation. *Prog Aerosp Sci* 2013;57:25–70.
21. Wang KL, Zhou Z, Zhu XP, et al. Aerodynamic design of multi-propeller/wing integration at low Reynolds numbers. *Aerosp Sci Technol* 2019;84:1–17.
22. Wang KL, Zhou Z, Fan ZY, et al. Aerodynamic design of tractor propeller for high-performance distributed electric propulsion aircraft. *Chin J Aeronaut* 2021;34(10):20–35.
23. Guo JH, Zhou Z. Multi-objective design of a distributed ducted fan system. *Aerospace* 2022;9(3):165.
24. Ma TL, Wang XS, Qiao NX, et al. A conceptual design and optimization approach for distributed electric propulsion eVTOL aircraft based on ducted-fan wing unit. *Aerospace* 2022;9(11):690.
25. de Vries R, van Arnhem N, Sinnige T, et al. Aerodynamic interaction between propellers of a distributed-propulsion system in forward flight. *Aerosp Sci Technol* 2021;118:107009.
26. Zhang XY, Zhang W, Li WL, et al. Experimental research on aero-propulsion coupling characteristics of a distributed electric propulsion aircraft. *Chin J Aeronaut* 2023;36(2):201–12.
27. Barlow JB, Rae WH, Pope A, et al. *Low-speed wind tunnel testing*. New York: Wiley; 1999. p. 19–29.
28. Sforza PM. *Theory of aerospace propulsion*. Amsterdam: Elsevier; 2017. p. 487–524.